Journal of Computational Physics **151,** 816–835 (1999)
Article ID jcph.1999.6221, available online at http://www.idealibrary.com on IDEAL®

A Lattice Gas Automaton Capable of Modeling Three-Dimensional Electromagnetic Fields

Neil R. S. Simons,* Greg E. Bridges,† and Michel Cuhaci*

**Advanced Antenna Technology, VPRS, Communications Research Centre, 3701 Carling Avenue, P.O. Box 11490, Station H, Ottawa, Ontario, Canada K2H 8S2; †Department of Electrical and Computer Engineering, University of Manitoba, Winnipeg, Manitoba, Canada R3T 2N2*
E-mail: neil.simons@crc.ca

Received May 12, 1998; revised January 26, 1999

A lattice gas automaton (LGA) capable of modeling Maxwell's equations in three dimensions is described. The automaton is a three-dimensional interconnection of two-dimensional LGA cells, with appropriate operations at the junctions between cells to include the properties of polarization. A homogeneous mathematical description of the heterogeneous three-dimensional automaton is provided in terms of the underlying binary variables. The dynamics of the automaton conserve the scalar components of the electric and magnetic fields. The implementation of the automaton on the CAM-8 cellular automata machine is described. The LGA has been validated through calculation of resonant frequencies within various cavities. The numerical results indicate the success of the automaton in analyzing three-dimensional EM field problems. We have not proven analytically that this model reproduces Maxwell's equations in the macroscopic limit, as this is a topic of future study. © 1999 Academic Press

Key Words: computational electromagnetics; lattice gas automata.

I. INTRODUCTION

Our goal is not only to solve Maxwell's equations, but to accomplish this using low precision integer arithmetic. Our motivation is that this style of algorithm is ideally suited for implementation on fine-grain parallel computers. Special purpose fine-grain computing architectures, such as the CAM-8 cellular automata machine, already exist [1]. Operations within these types of architectures require very few bits of memory, and simple logical hardware or look-up tables can be used for fast evaluation. This approach is unlike the real number finite difference time domain (FDTD) [2], finite element (FE) [3], or transmission line matrix (TLM) [4] methods that have been widely applied to the solution of spatially heterogeneous electromagnetic (EM) field problems. These algorithms require floating point

0021-9991/99 $30.00

processors. Lattice gas automata (LGA) have been previously developed for modeling the behavior of complex fluids [5] and are extremely well suited for execution on machines such as CAM-8. LGA are represented by an extremely large regular lattice of interconnected cells. The cells are very simple, usually with only a few bits being used to define all possible operating states, and are updated in synchronism according to the same deterministic rule that is local spatially and temporally. In this paper, a LGA for Maxwell's equations is presented. The approach is applicable to "resonant" EM field problems where the wavelength of interest is on the same order as the characteristic length scale of the problem.

Any system, of moving particles (bits) on a lattice, in which conservation of mass and momentum are satisfied, will exhibit some form of fluid behavior. Depending on the underlying lattice and the selection of collision operator, the behavior may not be exactly that of a true physical fluid system as governed by the Navier–Stokes equation, but aspects of the qualitative behavior of a fluid will still be valid. As an example, the Hardy, de Pazzis, and Pomeau (HPP) LGA which adequately models linear acoustics (not considering viscous damping) does not model the Navier–Stokes equation properly [6]. Such a system is therefore inappropriate for accurately modeling fluid dynamics. However, the system may still be appropriate as a model of linear acoustics, as governed by the linear wave equation. Thus, ignoring the effect of an anisotropic viscosity, which will be discussed in Section IV, the HPP automaton is capable of modeling linear wave behavior and many variations of the HPP automaton are capable of modeling different sound speeds [7]. These HPP automata are therefore also capable of modeling two-dimensional electromagnetism [8, 9]. However, most practical EM field problems are three-dimensional for which the solution of Maxwell's equations is required.

Three-dimensional electromagnetism is described by the *vector* wave equation, and consequently an attempt to describe it using an acoustic analogy with only *scalar* wave phenomena is insufficient. For three-dimensional EM field problems, rules capable of yielding vector wave behavior are required where the macroscopic density and flow perturbations of selected sets of particles within the LGA obey the coupled partial differential equation form of Maxwell's equations,

$$\varepsilon\frac{\partial\bar{E}}{\partial t} = \nabla\times\bar{H}, \qquad \mu\frac{\partial\bar{H}}{\partial t} = \nabla\times\bar{E} \tag{1a}$$

where $\bar{E}$ is the electric field vector, $\bar{H}$ is the magnetic field vector, ε is the permittivity, and μ the permeability. In Cartesian coordinates (1a) can be expressed as

$$\frac{\partial E_x}{\partial t} = \frac{1}{\varepsilon}\left(\frac{\partial H_z}{\partial y} - \frac{\partial H_y}{\partial z}\right), \qquad \frac{\partial E_y}{\partial t} = \frac{1}{\varepsilon}\left(\frac{\partial H_x}{\partial z} - \frac{\partial H_z}{\partial x}\right), \qquad \frac{\partial E_z}{\partial t} = \frac{1}{\varepsilon}\left(\frac{\partial H_y}{\partial x} - \frac{\partial H_x}{\partial y}\right)$$
$$\frac{\partial H_x}{\partial t} = \frac{1}{\mu}\left(\frac{\partial E_y}{\partial z} - \frac{\partial E_z}{\partial y}\right), \qquad \frac{\partial H_y}{\partial t} = \frac{1}{\mu}\left(\frac{\partial E_z}{\partial x} - \frac{\partial E_x}{\partial z}\right), \qquad \frac{\partial H_z}{\partial t} = \frac{1}{\mu}\left(\frac{\partial E_x}{\partial y} - \frac{\partial E_y}{\partial x}\right). \tag{1b}$$

There are a large variety of possible LGA mesh topologies, the complexity of which depends on the fluid phenomena that is desired. Fortunately, simple lattice geometries can be employed if solving three-dimensional scalar acoustics is the only requirement. The simplest automaton capable of modeling the three-dimensional scalar wave equation requires only six particles per cell, where each particle possesses a unit mass and travels with speed $\Delta l/\Delta t$ (i.e., one mesh step, Δl in one time step, Δt). This automaton can be considered as a three-dimensional version of the HPP automaton, where the lattice is aligned with the Cartesian coordinates and consists of particles with identical mass and propagation speed.

The four-particle and six-particle HPP automata possess sufficient isotropy to capture wave behavior in two and three dimensions, respectively. Therefore, these automata are capable of providing the appropriate linear wave behavior of electromagnetism, and the only requirement is the augmentation of their capabilities to capture the vector nature of Maxwell's equations. The more complex face-centered hypercube (FCHC) lattice [6] used for three-dimensional Navier–Stokes equations is not required here.

In the following section we outline several methods for representing EM fields on a three-dimensional lattice. Although LGA could be devised to make use of all of these representations, we select an expanded representation for the development of our automaton. In Section III, a homogeneous description of the LGA collision operator is provided. In Section IV, the validation of the LGA is described. In order to validate the automaton's ability to model Maxwell's equations, we have simultaneously simulated TE and TM modes within rectangular cavities for a given set of boundary conditions. Numerical results indicate that the resonant frequencies of both TE and TM modes are accurately predicted. While these numerical results validate our approach, we have not proved analytically that the model reproduces Maxwell's equations in the macroscopic limit. This proof is eventually necessary and is a topic of our current research. In Section V we examine the computational resources of the LGA and propose methods for improvement.

II. REPRESENTATION OF EM FIELDS ON A THREE-DIMENSIONAL LATTICE

The differential equation based computational EM literature contains a variety of approaches for the spatial organization of a unit cell. Several different strategies based on these existing approaches for the spatial organization of the unit cell of our new LGA have been considered. A method for representing EM fields on a spatial lattice is required which accounts for the nature of LGA and enables efficient implementation in a fine-grain computing architecture such as the CAM-8 cellular automata machine.

For all differential equation based methods, including LGA, the volume of space enclosing the EM fields is discretized into unit cells. The spatial organization of the unit cell is closely related to the method of discretization. It is, however, possible to use an arbitrary spatial cell organization with a variety of discretization techniques (i.e., finite difference, finite element, finite volume). Here, we classify the various spatial organizations of the unit cells in terms of two parameters: *symmetry* and *condensation*. A *symmetric* cell appears the same (in terms of the vector components of the fields) from each coordinate axis. A *condensed* cell has all field components defined at the same spatial locations. A completely uncondensed cell has only a single field component defined at a given spatial location, and a partially condensed cell has some, but not all, field components defined at a given spatial location. Examples of the spatial organizations of unit cells are presented in Fig. 1.

In the computational EM literature, many of the spatial organizations of unit cubic cells shown in Fig. 1 have become associated with specific numerical discretization schemes. For example, the expanded representation of Fig. 1a has become associated with the generic term "finite difference time domain" [2]. However, such rigid association is not necessary and it is possible to formulate finite difference algorithms based on all of the discretizations

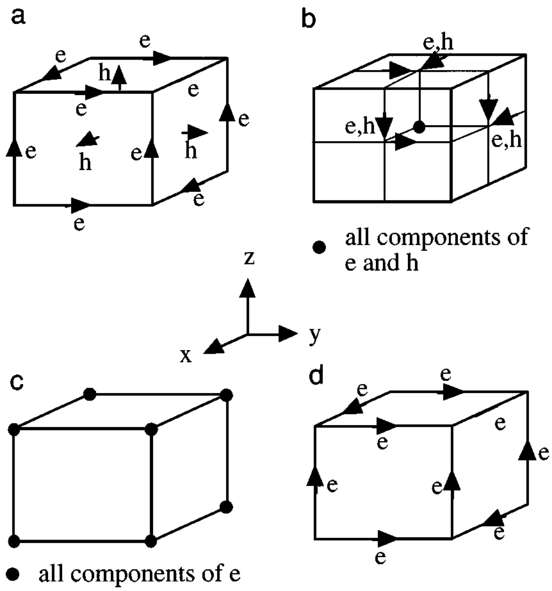

FIG. 1. Spatial organization of unit cubic cell. (a) Yee finite-difference algorithm [14] and the expanded node transmission line matrix model [10] (unsymmetrical, uncondensed); (b) transmission line matrix algorithm [11] and Shankar finite-volume algorithm [15] (symmetric, partially condensed); (c) nodal-based finite-element method (symmetric, condensed); (d) edge-element finite-element methods (symmetric, partially condensed).

of Fig. 1. It is a more fundamental methodology to differentiate the mesh representation from the numerical discretization. It is also possible to formulate TLM schemes with all of the cells shown in Fig. 1. The original TLM scheme employs the spatial cell of Fig. 1a [10]. The so-called symmetric condensed node TLM scheme [11], which is actually partially condensed, utilizes the unit cell of Fig. 1b. The three-dimensional extension of the hybrid finite-element/TLM algorithm presented in [12] would require the unit cell of Fig. 1c.

Given the above classification of EM field representations on three-dimensional lattices, our goal is to develop a LGA utilizing one of these spatial organizations. Current LGA are based on the interaction of particles, which have the properties of mass, and due to their direction of propagation, momentum. The automaton is based on the interaction of particles having the properties of mass, momentum, and polarization. Each particle possessing a ξ-polarization contributes to the ξ component of the macroscopic electric field, where $\xi \in (x, y, z)$. The particles on this lattice would conserve mass and momentum and interact according to their polarization. In this manner, the LGA appears as a TLM-like algorithm in which single-bit variables are used.

An LGA implementation of the *symmetric-condensed* lattice as shown in Fig. 1c with a complete set of ξ-polarized particles at each spatial location and a unit cell would require 36 particles. A LGA implementation on the *symmetric*, *partially condensed* lattice shown in Fig. 1d would require 24 particles. The spatial organizations for these two cases with required particles are provided in Fig. 2. Each node location (•) in Fig. 1c corresponds with a spatial location at which the dashed lines intersect in Fig. 2a. The spatial locations in Fig. 2a at which the particles are shown correspond to spatial locations half-way between the nodes of Fig. 1c. The node location (•) in Fig. 1b corresponds with the intersection of solid lines in Fig. 2b. The spatial locations in Fig. 2b at which the particles are shown

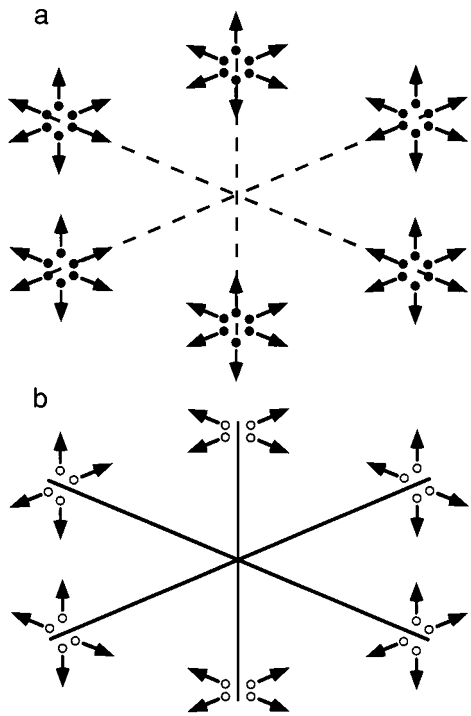

FIG. 2. Spatial organization of unit cells including the required particles for the three-dimensional LGA cell constructed from (a) the symmetric condensed cell of Fig. 1c requiring 36 particles, and (b) the symmetric partially condensed cell of Fig. 1b requiring 24 particles.

correspond to spatial locations at which the tangential fields are defined in Fig. 1c. Since only tangential fields are defined between nodal locations in Figs. 2b and 1b, only particles carrying tangential fields are required.

A problem with both spatial organizations of Fig. 2 is that a fairly large number of bits are required per unit cell. The main motivation for the LGA approach is to enable operation as a fine-grain computing system and thus minimization of the number of bits per unit cell is imperative. For example, the CAM-8 cellular automata machine performs collision operations using a 16-bit look-up table and thus operates most efficiently on 16 bits of state per site at any instant of time. Implementations involving cell sizes of more than 16 bits can be accommodated by parsing the particle interactions into 16-bit operations, but this becomes computationally cumbersome. In general, an n-bit collision process requires a 2^n sized look-up table. If an n-bit collision operator look-up table must be parsed in a brute-force manner into 16-bit operations, 2^m look-up tables are required for an $\mathrm{m} + 16$ bit collision operator. It is therefore desirable to exploit any symmetries of the lattice or factorizations to parse a collision operator involving more than 16 bits. For example, in [13] the implementation of an FCHC LGA on CAM-8 is described. The FCHC LGA requires 24 particles per cell, however, Adler *et al*. were able to split the 24-bit collision process into two 16-bit collision events. Instead of searching for a similar reduction of the collision process for either of the 36- or 24-bit automata of Fig. 2, we have selected an *unsymmetrical, uncondensed* (or expanded) lattice. This reduces the number of bits required at each CAM-8 site to less than 16 bits. In fact, the number of particles per CAM-8 site is reduced to 8, if one site is assigned to each electric or magnetic field component as shown in Fig. 1a. Therefore, 6 CAM-8 sites are required for a complete unit cell based on the spatial organization of Fig. 1a. The CAM-8 implementation of the automaton is described in Subsection III.3.

III. NEW THREE-DIMENSIONAL VECTOR LATTICE GAS AUTOMATON FOR MAXWELL'S EQUATIONS

III.1. *Spatial Organization of the New Automaton*

The state of a cell at discrete (integer indexed) spatial locations $\mathbf{x} = (x, y, z)$ in three-dimensional space and at time t is given by

$$s(\mathbf{x}, t) = B(\mathbf{x}, t) = \begin{Bmatrix} b^+_{+x}(\mathbf{x}, t), b^+_{+y}(\mathbf{x}, t), b^+_{+z}(\mathbf{x}, t), b^+_{-x}(\mathbf{x}, t), b^+_{-y}(\mathbf{x}, t), b^+_{-z}(\mathbf{x}, t), \\ b^-_{+x}(\mathbf{x}, t), b^-_{+y}(\mathbf{x}, t), b^-_{+z}(\mathbf{x}, t), b^-_{-x}(\mathbf{x}, t), b^-_{-y}(\mathbf{x}, t), b^-_{-z}(\mathbf{x}, t) \end{Bmatrix} \quad (2)$$

or more concisely as

$$s(\mathbf{x}, t) = B(\mathbf{x}, t) = \left\{ b^\pm_{\pm x}(\mathbf{x}, t), b^\pm_{\pm y}(\mathbf{x}, t), b^\pm_{\pm x}(\mathbf{x}, t) \right\},$$

where the particles of our automaton are described using binary variables, $b^\pm_{\pm\xi} \in \{0, 1\}$. The $\pm$ superscript denotes a positive or a negative particle, and $\pm\xi$ denotes a particle travelling in the $\pm\xi$ direction, where $\xi \in \{x, y, z\}$. Equation (2) has been constructed using 12 particles per lattice site. We will eventually show that due to the parity operators, only 8 particles are required. In this document, since binary variables are used, the algebra utilizes the Boolean AND, OR, and NOT operations. The operations, defined on two variables a and b, are ab (AND), $a + b$ (OR), $\overline{a}$ (NOT). A site specific operator is not used in the description of the particles. Here we only use a polarity (positive or negative particle) identifier and a propagation direction identifier. Using this notation, we require additional information in order to define the field quantities associated with the lattice particles.

The description given by Eq. (2) of the automaton allows particles to exist in all velocity states at all spatial locations within the lattice. We will now define an expanded-style unsymmetrical uncondensed lattice as in Fig. 1a using the 12-particle cell of (2). This will be accomplished by defining parity operators which exclude particles from occupying illegal states. The parity operators are defined as

$$p_\xi = \left\| \begin{matrix} 0 & \text{if } \xi \text{ is even} \\ 1 & \text{if } \xi \text{ is odd} \end{matrix} \right. \quad \text{for } \xi \in (x, y, z). \quad (3)$$

Based on the interpretation of the expanded mesh of Fig. 1a, each E or H field site in the lattice should be associated with specific "polarized" particles. For example, $+\xi$ polarized particles will be associated with $+$ superscripts and contribute to the macroscopic E_ξ field component while $-\xi$ polarized particles subtract from it, where $\xi \in (x, y, z)$. To conform to the expanded lattice, we restrict the particles to represent microscopic TEM propagators, and therefore the ξ direction is perpendicular to the direction of propagation of the $\pm\xi$ polarized particles. Based on this interpretation, the fields at the various spatial locations of the expanded mesh can be defined as

$$\begin{aligned} E_x = {} & p_x p_y \overline{p}_z \left(b^+_{+y} + b^+_{-y} + b^+_{+z} + b^+_{-z} - b^-_{+y} - b^-_{-y} - b^-_{+z} - b^-_{-z} \right) \\ & + p_x p_y p_z \left(b^+_{+z} - b^+_{-z} + b^-_{+z} + b^-_{-z} \right) + p_x \overline{p}_y \overline{p}_z \left(-b^+_{+y} + b^+_{-y} + b^-_{+y} - b^-_{-y} \right) \quad (4a) \end{aligned}$$

$$E_y = \bar{p}_x \bar{p}_y \bar{p}_z \left(b^+_{+x} + b^+_{-x} + b^+_{+z} + b^+_{-z} - b^-_{+x} - b^-_{-x} - b^-_{+z} - b^-_{-z}\right)$$
$$+ \bar{p}_x \bar{p}_y p_z \left(- b^+_{+z} + b^+_{-z} + b^-_{+z} - b^-_{-z}\right) + p_x \bar{p}_y \bar{p}_z \left(b^+_{+x} - b^+_{-x} - b^-_{+x} + b^-_{-x}\right) \quad (4b)$$

$$E_z = \bar{p}_x p_y p_z \left(b^+_{+x} + b^+_{-x} + b^+_{+y} + b^+_{-y} - b^-_{+x} - b^-_{-x} - b^-_{+y} - b^-_{-y}\right)$$
$$+ \bar{p}_x \bar{p}_y p_z \left(b^+_{+y} - b^+_{-y} + b^-_{+y} + b^-_{-y}\right) + p_x p_y p_z \left(-b^+_{+x} + b^+_{-x} + b^-_{+x} - b^-_{-x}\right) \quad (4c)$$

$$H_x = \bar{p}_x \bar{p}_y p_z \left(b^+_{+y} + b^+_{-y} + b^+_{+z} + b^+_{-z} - b^-_{+y} - b^-_{-y} - b^-_{+z} - b^-_{-z}\right)$$
$$+ \bar{p}_x \bar{p}_y \bar{p}_z \left(-b^+_{+z} + b^+_{-z} + b^-_{+z} - b^-_{-z}\right) + \bar{p}_x p_y p_z \left(+b^+_{+y} - b^+_{-y} - b^-_{+y} + b^-_{-y}\right) \quad (4d)$$

$$H_y = p_x p_y p_z \left(b^+_{+x} + b^+_{-x} + b^+_{+z} + b^+_{-z} - b^-_{+x} - b^-_{-x} - b^-_{+z} - b^-_{-z}\right)$$
$$+ p_x p_y \bar{p}_z \left(+b^+_{+z} - b^+_{-z} - b^-_{+z} + b^-_{-z}\right) + \bar{p}_x p_y p_z \left(-b^+_{+x} + b^+_{-x} + b^-_{+x} - b^-_{-x}\right) \quad (4e)$$

$$H_z = p_x \bar{p}_y \bar{p}_z \left(b^+_{+x} + b^+_{-x} + b^+_{+y} + b^+_{-y} - b^-_{+x} - b^-_{-x} - b^-_{+y} - b^-_{-y}\right)$$
$$+ p_x p_y \bar{p}_z \left(-b^+_{+y} + b^+_{-y} - b^-_{+y} - b^-_{-y}\right) + \bar{p}_x \bar{p}_y \bar{p}_z \left(-b^+_{+x} + b^+_{-x} + b^-_{+x} - b^-_{-x}\right). \quad (4f)$$

The resulting expanded style mesh is as shown in Figs. 3 and 4.

In (2), there is no need to denote the field component to which the particle contributes, since this is determined by the parity operator (3) and spatial coordinates of the site. A valid propagation direction $\hat{d}$ for a particle at an E_ξ or H_ξ site is any non-zero outcome of the operation $\hat{d} \times \hat{\xi}$. Again, this is because the particles represent TEM propagators. To illustrate our definitions of particles, four particles within a unit cell of the automaton are provided in Fig. 4.

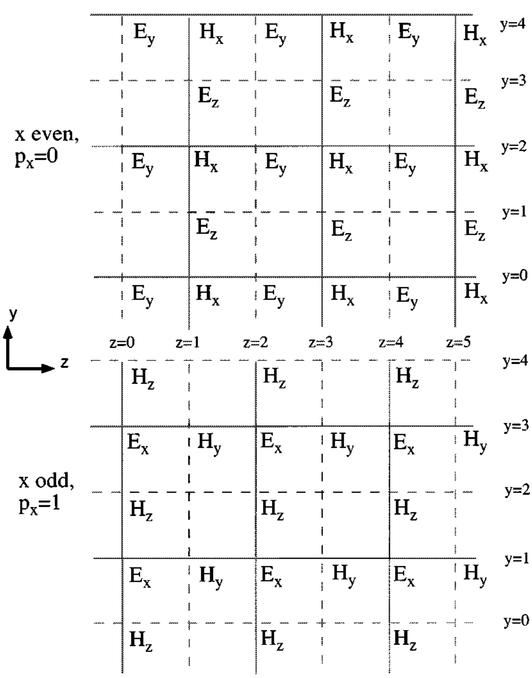

FIG. 3. Visualization of two cuts of the lattice in the $y - z$ plane. These cuts are at $x = x_0 \Delta l$ and $x = (x_0+1)\Delta l$. Both here and in Fig. 4, the solid lines indicate paths along which particles may propagate, and dashed lines indicate paths along which particles may not propagate.

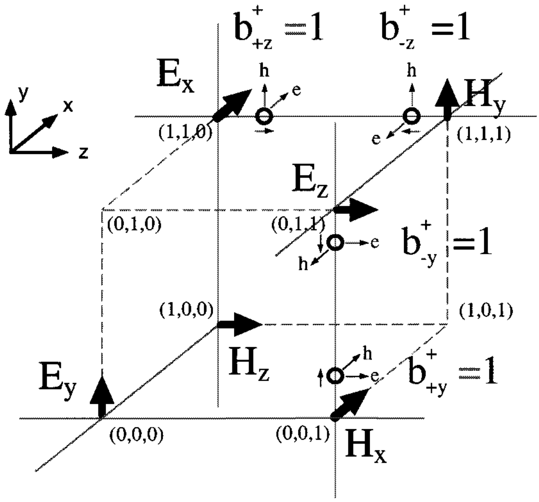

FIG. 4. A single expanded three-dimensional cell indicating the spatial organization of the E and H field sites and their relation to the particles. This expanded mesh implementation occupies a space of 2^3 CAM-8 sites. Positive E_x and H_y particles are shown propagating from the E_x to H_y, and H_y to E_x sites, respectively. Positive E_z and H_x particles are shown propagating from the E_z to H_x, and H_x to E_z sites, respectively. The front face ($x = 0$) and the back face ($x = 1$) can be seen as a portion of the planes of Fig. 3.

Two cuts through the lattice in the $y - z$ plane are shown in Fig. 3, and a complete unit cell is provided in Fig. 4. The unit cell shown in Fig. 4 occupies a cube with a side length of 2 Δl. The distance from an E_ξ site to the next occurrence of an E_ξ site is 2 Δl. In Figs. 3 and 4, the sites are labeled by the field component represented by a particular site. At an E_ξ site, all the particles contribute to the ξ-component of the electric field. A site is required for each Cartesian component of the electric and magnetic fields (E_x, E_y, E_z, H_x, H_y, H_z). For this particular automaton, only microscopic transverse electromagnetic (TEM) propagators exist. Therefore, ξ-polarized particles do not travel in the ξ direction. In both of these figures, the solid lines indicate the presence of interconnections or paths along which the particles travel. The dashed lines are placed for visualization to represent paths along which particles are not allowed to travel. The intersections of dashed lines represent locations where particles are not allowed to exist. Because of this restriction, a specific spatial organization of sites is required in order to connect the three electric and the three magnetic field sites. This spatial organization is the expanded unsymmetrical spatial organization of Fig. 1a. The site labels are given in terms of the parity operator (3) in Table I. Also provided in Table I are the correspondence between net particle density (positive particles–negative particles), net momentum, and field quantities. This additional information aids in the understanding of the field definitions (4). The two null sites are spatial locations at which particles do not exist. An explanation of how the lattice of Fig. 3 and unit cell of Fig. 4 relate to the Cartesian representation of Maxwell's equations (1b) is given at the end of Subsection III.2.

III.2. *Operation of the Automaton*

Based on the above description of the geometry of the LGA, the operation of the LGA can be now described in the usual manner in terms of collision and advection events [6].

TABLE I
Specification of Site Locations in Terms of Parity Operators and Relevant Electromagnetic Field Quantities

Site label	p_x	p_y	p_z	Particle density	x-momentum	y-momentum	z-momentum
E_x	$p_x = 1$	$p_y = 1$	$p_z = 0$	E_x	NA	$-H_z$	H_y
E_y	$p_x = 0$	$p_y = 0$	$p_z = 0$	E_y	H_z	NA	$-H_x$
E_z	$p_x = 0$	$p_y = 1$	$p_z = 1$	E_z	$-H_y$	H_x	NA
H_x	$p_x = 0$	$p_y = 0$	$p_z = 1$	H_x	NA	E_z	$-E_y$
H_y	$p_x = 1$	$p_y = 1$	$p_z = 1$	H_y	$-E_z$	NA	E_x
H_z	$p_x = 1$	$p_y = 0$	$p_z = 0$	H_z	E_y	$-E_x$	NA
Null	$p_x = 1$	$p_y = 0$	$p_z = 1$	NA	NA	NA	NA
Null	$p_x = 0$	$p_y = 1$	$p_z = 0$	NA	NA	NA	NA

The dynamics of the LGA are defined as

$$b^{\pm}_{\pm\xi}(\mathbf{x} \pm \mathbf{c}_\xi \Delta l, t + \Delta t) = b^{\pm}_{\pm\xi}(\mathbf{x}, t) + C^{\pm}_{\pm\xi}(B(\mathbf{x}, t)), \tag{5}$$

where $C^{\pm}_{\pm\xi}$ is the collision operator for the particles travelling in the $\pm\xi$ direction, and $\xi \in (x, y, z)$. Equation (5) can be interpreted as defining the states of the lattice at time $t + \Delta t$ in terms of the states at time t. Here, the particles propagate with speed $1\Delta l$ per Δt. This collision operator includes the effects of both the collision and the polarization event. In order to separate the polarization and collision events intermediate variables are employed. The intermediate variables are denoted as $\grave{b}^{\pm}_{\pm\eta}$, which are the bit values after the collision operation, but before the polarization event. Therefore, the lattice dynamics can also be defined as

$$\grave{b}^{\pm}_{\pm\eta}(\mathbf{x} \pm \mathbf{c}_\eta \Delta l, t + \Delta t) = b^{\pm}_{\pm\eta}(\mathbf{x}, t) + \grave{C}^{\pm}_{\pm\eta}(B(\mathbf{x}, t)) \tag{6a}$$

$$b^{\pm}_{\pm\eta}(\mathbf{x}, t) = T^{\pm}_{\pm\eta}(\grave{B}(\mathbf{x}, t)), \tag{6b}$$

where the operator $\grave{C}$ describes the collision event without the polarization event, and the operator T describes the polarization event. HPP collision rules are applied [16], and using the above notation, the collision event is given as

$$\grave{b}^{\pm}_{\pm x}(x \pm \Delta l, y, z, t + \Delta t) = b^{\pm}_{\pm x}(\mathbf{x}, t) + \grave{C}^{\pm}_{\pm x}(B(\mathbf{x}, t)), \tag{7a}$$

$$\grave{b}^{\pm}_{\pm y}(x, y \pm \Delta l, z, t + \Delta t) = b^{\pm}_{\pm y}(\mathbf{x}, t) + \grave{C}^{\pm}_{\pm y}(B(\mathbf{x}, t)), \tag{7b}$$

$$\grave{b}^{\pm}_{\pm z}(x, y, z \pm \Delta l, t + \Delta t) = b^{\pm}_{\pm z}(\mathbf{x}, t) + \grave{C}^{\pm}_{\pm z}(B(\mathbf{x}, t)), \tag{7c}$$

where

$$\grave{C}^{\pm}_{\pm x}(B(\mathbf{x}, t)) = (p_x p_y p_z + \overline{p}_x \overline{p}_y \overline{p}_z)\Theta^{\pm}_{xz} + (p_x \overline{p}_y \overline{p}_z + \overline{p}_x p_y p_z)\Theta^{\pm}_{xy},$$

$$\grave{C}^{\pm}_{\pm y}(B(\mathbf{x}, t)) = (p_x \overline{p}_y \overline{p}_z + \overline{p}_x p_y p_z)\Theta^{\pm}_{yx} + (p_x p_y \overline{p}_z + \overline{p}_x \overline{p}_y p_z)\Theta^{\pm}_{yz},$$

$$\grave{C}^{\pm}_{\pm z}(B(\mathbf{x}, t)) = (p_x p_y p_z + \overline{p}_x \overline{p}_y \overline{p}_z)\Theta^{\pm}_{zx} + (p_x p_y \overline{p}_z + \overline{p}_x \overline{p}_y p_z)\Theta^{\pm}_{zy},$$

and

$$\Theta^{\pm}_{\eta\xi} = \left(\overline{b}^{\pm}_{+\eta}\overline{b}^{\pm}_{-\eta} b^{\pm}_{+\xi} b^{\pm}_{-\xi} - b^{\pm}_{+\eta} b^{\pm}_{-\eta}\overline{b}^{\pm}_{+\xi}\overline{b}^{\pm}_{-\xi}\right), \qquad \text{where } \eta, \xi \in (x, y, z).$$

The particle states in the definition for $\Theta^{\pm}_{\eta\xi}$ given above are evaluated at $(\mathbf{x}, t)$. The above collision operator is homogeneous, thus is applicable at every spatial location throughout the lattice. The parity operators, p_ξ, are used to specify the appropriate spatial locations at which the appropriate particle interactions occur. These terms specify the spatial heterogeneity of the lattice as shown in Figs. 3 and 4 within a homogeneous particle description (2).

It must be noted that in the description of the collision operator (7), $+\xi$ particles do not interact with $-\xi$ particles and *vice versa*. The HPP collision operator defined in (7) as $\Theta^{\pm}_{\eta\xi}$ is succinctly described as particles which do not interact, except for pairwise head-on collisions; for pairwise head-on collisions, the resultant particles are transformed 90° to the original pair [6].

Operation (6a) is applied at all sites within the lattice to obtain the values $\grave{b}$ throughout the entire mesh. These values are then transferred to adjacent sites, via the polarization operation (6b), to obtain the new states of the automaton, b.

Again, due to the spatial organization shown in Figs. 3 and 4, the polarization event is spatially heterogeneous and requires the parity operators in order to be described in a homogeneous manner. The polarization event is given as

$$
\begin{aligned}
b^{\pm}_{+x}(\mathbf{x}, t) &= \bar{p}_y \bar{p}_z \grave{b}^{\pm}_{+x}(\mathbf{x}, t) + p_y p_z \grave{b}^{\mp}_{+x}(\mathbf{x}, t)\\
b^{\pm}_{-x}(\mathbf{x}, t) &= p_y p_z \grave{b}^{\pm}_{-x}(\mathbf{x}, t) + \bar{p}_y \bar{p}_z \grave{b}^{\mp}_{-x}(\mathbf{x}, t)\\
b^{\pm}_{+y}(\mathbf{x}, t) &= \bar{p}_x p_z \grave{b}^{\pm}_{+y}(\mathbf{x}, t) + p_x \bar{p}_z \grave{b}^{\mp}_{+y}(\mathbf{x}, t)\\
b^{\pm}_{-y}(\mathbf{x}, t) &= p_x \bar{p}_z \grave{b}^{\pm}_{-y}(\mathbf{x}, t) + \bar{p}_x p_z \grave{b}^{\mp}_{-y}(\mathbf{x}, t)\\
b^{\pm}_{+z}(\mathbf{x}, t) &= p_x p_y \grave{b}^{\pm}_{+z}(\mathbf{x}, t) + \bar{p}_x \bar{p}_y \grave{b}^{\mp}_{+z}(\mathbf{x}, t)\\
b^{\pm}_{-z}(\mathbf{x}, t) &= \bar{p}_x \bar{p}_y \grave{b}^{\pm}_{-z}(\mathbf{x}, t) + p_x p_y \grave{b}^{\mp}_{-z}(\mathbf{x}, t).
\end{aligned} \tag{8a}
$$

Operation (8a) is invariant with respect to shifts in space or time, and can be rewritten as

$$
\begin{aligned}
&b^{\pm}_{+x}(x + \Delta l, y, z, t + \Delta t)\\
&\quad = \bar{p}_y \bar{p}_z \grave{b}^{\pm}_{+x}(x + \Delta l, y, z, t + \Delta t) + p_y p_z \grave{b}^{\mp}_{+x}(x + \Delta l, y, z, t + \Delta t)\\
&b^{\pm}_{-x}(x - \Delta l, y, z, t + \Delta t)\\
&\quad = p_y p_z \grave{b}^{\pm}_{-x}(x - \Delta l, y, z, t + \Delta t) + \bar{p}_y \bar{p}_z \grave{b}^{\mp}_{-x}(x - \Delta l, y, z, t + \Delta t)\\
&b^{\pm}_{+y}(x, y + \Delta l, z, t + \Delta t)\\
&\quad = \bar{p}_x p_z \grave{b}^{\pm}_{+y}(x, y + \Delta l, z, t + \Delta t) + p_x \bar{p}_z \grave{b}^{\mp}_{+y}(x, y + \Delta l, z, t + \Delta t)\\
&b^{\pm}_{-y}(x, y - \Delta l, z, t + \Delta t)\\
&\quad = p_x \bar{p}_z \grave{b}^{\pm}_{-y}(x, y - \Delta l, z, t + \Delta t) + \bar{p}_x p_z \grave{b}^{\mp}_{-y}(x, y - \Delta l, z, t + \Delta t)\\
&b^{\pm}_{+z}(x, y, z + \Delta l, t + \Delta t)\\
&\quad = p_x p_y \grave{b}^{\pm}_{+z}(x, y, z + \Delta l, t + \Delta t) + \bar{p}_x \bar{p}_y \grave{b}^{\mp}_{+z}(x, y, z + \Delta l, t + \Delta t)\\
&b^{\pm}_{-z}(x, y, z - \Delta l, t + \Delta t)\\
&\quad = \bar{p}_x \bar{p}_y \grave{b}^{\pm}_{-z}(x, y, z - \Delta l, t + \Delta t) + p_x p_y \grave{b}^{\mp}_{-z}(x, y, z - \Delta l, t + \Delta t).
\end{aligned} \tag{8b}
$$

We can now substitute (7) into the above polarization event (8b), to obtain

$$\begin{aligned}
b^{\pm}_{+x}(x+\Delta l, y, z, t+\Delta t) &= \bar{p}_y \bar{p}_z \left(b^{\pm}_{+x}(\mathbf{x}, t) + \grave{C}^{\pm}_{+x}\right) + p_y p_z \left(b^{\mp}_{+x}(\mathbf{x}, t) + \grave{C}^{\mp}_{+x}\right)\\
b^{\pm}_{-x}(x-\Delta l, y, z, t+\Delta t) &= p_y p_z \left(b^{\pm}_{-x}(\mathbf{x}, t) + \grave{C}^{\pm}_{-x}\right) + \bar{p}_y \bar{p}_z \left(b^{\mp}_{-x}(\mathbf{x}, t) + \grave{C}^{\mp}_{-x}\right)\\
b^{\pm}_{+y}(x, y+\Delta l, z, t+\Delta t) &= \bar{p}_x p_z \left(b^{\pm}_{+y}(\mathbf{x}, t) + \grave{C}^{\pm}_{+y}\right) + p_x \bar{p}_z \left(b^{\mp}_{+y}(\mathbf{x}, t) + \grave{C}^{\mp}_{+y}\right)\\
b^{\pm}_{-y}(x, y-\Delta l, z, t+\Delta t) &= p_x \bar{p}_z \left(b^{\pm}_{-y}(\mathbf{x}, t) + \grave{C}^{\pm}_{-y}\right) + \bar{p}_x p_z \left(b^{\mp}_{-y}(\mathbf{x}, t) + \grave{C}^{\mp}_{-y}\right)'\\
b^{\pm}_{+z}(x, y, z+\Delta l, t+\Delta t) &= p_x p_y \left(b^{\pm}_{+z}(\mathbf{x}, t) + \grave{C}^{\pm}_{+z}\right) + \bar{p}_x \bar{p}_y \left(b^{\mp}_{+z}(\mathbf{x}, t) + \grave{C}^{\mp}_{+z}\right)\\
b^{\pm}_{-z}(x, y, z-\Delta l, t+\Delta t) &= \bar{p}_x \bar{p}_y \left(b^{\pm}_{-z}(\mathbf{x}, t) + \grave{C}^{\pm}_{-z}\right) + p_x p_y \left(b^{\mp}_{-z}(\mathbf{x}, t) + \grave{C}^{\mp}_{-z}\right).
\end{aligned} \tag{9}$$

In order to obtain the dynamics of the form (5), we have to rearrange the terms in (9). Rearranging the collision event for $b^{\pm}_{+x}$ yields

$$\begin{aligned}
&b^{\pm}_{+x}(x+\Delta l, y, z, t+\Delta t)\\
&\quad= \bar{p}_y \bar{p}_z \left(b^{\pm}_{+x}(\mathbf{x}, t) + \grave{C}^{\pm}_{+x}\right) + p_y p_z \left(b^{\mp}_{+x}(\mathbf{x}, t) + \grave{C}^{\mp}_{+x}\right)\\
&\quad= \bar{p}_y \bar{p}_z b^{\pm}_{+x}(\mathbf{x}, t) + \bar{p}_y \bar{p}_z \grave{C}^{\pm}_{+x} + p_y p_z \left(b^{\mp}_{+x}(\mathbf{x}, t) + \grave{C}^{\mp}_{+x}\right)\\
&\quad= (1-p_y p_z) b^{\pm}_{+x}(\mathbf{x}, t) + (1-p_y p_z)\, \grave{C}^{\pm}_{+x} + p_y p_z \left(b^{\mp}_{+x}(\mathbf{x}, t) + \grave{C}^{\mp}_{+x}\right).
\end{aligned} \tag{10}$$

Adding and subtracting $p_y p_z b^{\pm}_{+x}(\mathbf{x}, t)$ from the RHS of (10) yields the appropriate form of the collision operator,

$$b^{\pm}_{+x}(x+\Delta l, y, z, t+\Delta t) = b^{\pm}_{+x}(\mathbf{x}, t) + C^{\pm}_{+x}, \tag{11a}$$

where

$$C^{\pm}_{+x} = \bar{p}_y \bar{p}_z \grave{C}^{\pm}_{+x} + (1-\bar{p}_y \bar{p}_z)\left(b^{\mp}_{+x}(\mathbf{x}, t) - b^{\pm}_{+x}(\mathbf{x}, t) + \grave{C}^{\mp}_{+x}\right). \tag{12a}$$

Similarly for the other particles,

$$\begin{aligned}
b^{\pm}_{-x}(x-\Delta l, y, z, t+\Delta t) &= b^{\pm}_{-x}(\mathbf{x}, t) + C^{\pm}_{-x}\\
b^{\pm}_{+y}(x, y+\Delta l, z, t+\Delta t) &= b^{\pm}_{+y}(\mathbf{x}, t) + C^{\pm}_{+y}\\
b^{\pm}_{-y}(x, y-\Delta l, z, t+\Delta t) &= b^{\pm}_{-y}(\mathbf{x}, t) + C^{\pm}_{-y}\\
b^{\pm}_{+z}(x, y, z+\Delta l, t+\Delta t) &= b^{\pm}_{+z}(\mathbf{x}, t) + C^{\pm}_{+z}\\
b^{\pm}_{-z}(x, y, z-\Delta l, t+\Delta t) &= b^{\pm}_{-z}(\mathbf{x}, t) + C^{\pm}_{-z},
\end{aligned} \tag{11b}$$

where

$$\begin{aligned}
C^{\pm}_{-x} &= p_y p_z \grave{C}^{\pm}_{-x} + (1-p_y p_z)\left(b^{\mp}_{-x}(\mathbf{x}, t) - b^{\pm}_{-x}(\mathbf{x}, t) + \grave{C}^{\mp}_{-x}\right)\\
C^{\pm}_{+y} &= \bar{p}_x p_z \grave{C}^{\pm}_{+y} + (1-\bar{p}_x p_z)\left(b^{\mp}_{+y}(\mathbf{x}, t) - b^{\pm}_{+y}(\mathbf{x}, t) + \grave{C}^{\mp}_{+y}\right)\\
C^{\pm}_{-y} &= p_x \bar{p}_z \grave{C}^{\pm}_{-y} + (1-p_x \bar{p}_z)\left(b^{\mp}_{-y}(\mathbf{x}, t) - b^{\pm}_{-y}(\mathbf{x}, t) + \grave{C}^{\mp}_{-y}\right)\\
C^{\pm}_{+z} &= p_x p_y \grave{C}^{\pm}_{+z} + (1-p_x p_y)\left(b^{\mp}_{+z}(\mathbf{x}, t) - b^{\pm}_{+z}(\mathbf{x}, t) + \grave{C}^{\mp}_{+z}\right)\\
C^{\pm}_{-z} &= \bar{p}_x \bar{p}_y \grave{C}^{\pm}_{-z} + (1-\bar{p}_x \bar{p}_y)\left(b^{\mp}_{-z}(\mathbf{x}, t) - b^{\pm}_{-z}(\mathbf{x}, t) + \grave{C}^{\mp}_{-z}\right).
\end{aligned} \tag{12b}$$

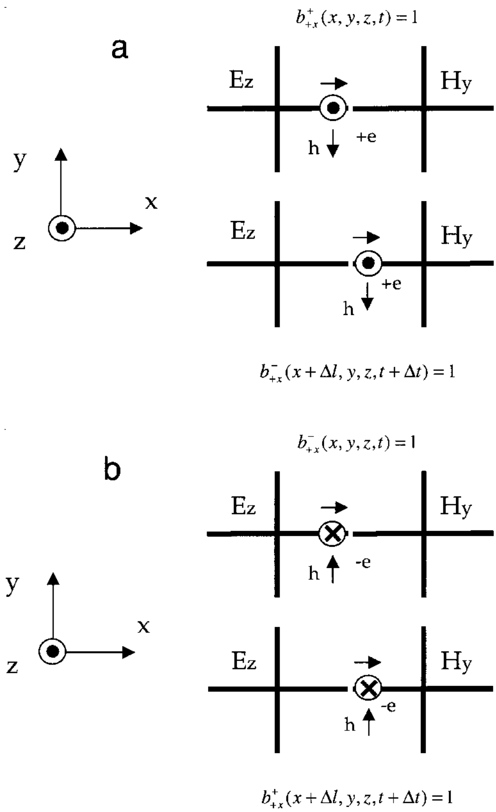

FIG. 5. The junction between two cells displaying $\pm E_z$ and $\pm H_y$ particles.

A particular example of the polarization event (8a) required to link all of the lattice sites that represent different electric and magnetic field components is provided in Fig. 5. Two adjacent sites in the $x - y$ plane are shown in Fig. 5 (an H_y and an E_z cell). At the junction between these sites, an operation is required to ensure consistent polarization as particles pass to an adjacent site. For instance, a positive E_z particle travelling in the $+x$ direction is transformed into a negative H_y particle when it enters the H_y site as shown in Fig. 5a. Similarly, a negative E_z particle travelling in the $+x$ direction is transformed into a positive H_y particle when it enters the H_y site as shown in Fig. 5b. A positive (negative) H_y particle travelling in the $-x$ direction remains a positive (negative) particle upon entering the E_z site. The special case of a single particle propagating through the lattice in the $+x$ direction is provided in Fig. 6. There are no other particles at the lattice sites and therefore following the HPP collision operation (embedded within (7)) the particle propagates through the mesh undisturbed. The particle exists as a positive particle at the E_z site at time t. It is transformed into a negative particle existing at the H_y site at time $t + \Delta t$, and subsequently becomes a positive particle at the E_z site at time $t + 2\Delta t$. Note that this special case is used to illustrate the transfer event and does not represent a configuration of the mesh that would lead to a particle solution of an EM field problem.

Each of the six sites which comprise the unit cell (labelled as E_x, E_y, E_z, H_x, H_y, H_z in Fig. 4), can be considered to model one of the six expressions in the Cartesian representation of Maxwell's equations (1b). For instance, the expression $\partial E_x/\partial t = (1/\varepsilon)(\partial H_z/\partial y - \partial H_y/\partial z)$ can be considered to be represented by the E_x field site. The E_x field component in the

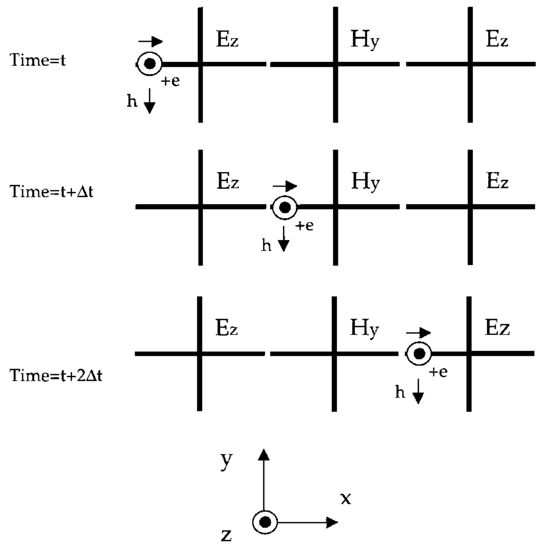

FIG. 6. Visualization of a single particle propagating through the mesh on successive time steps.

expression is linked to the H_y and H_z fields. In the unit cell of Fig. 4, the sites representing H_y and H_z are adjacent to the E_x site. The transformation events linking adjacent sites can be thought of as providing coupling between the six expressions representing the expression of Maxwell's equations in Cartesian coordinates. The dynamics of the automaton conserve each of the scalar components of the electric and magnetic fields. The conservation of these quantities is observed through inspection of the collision operator and the polarization event with respect to the definitions for the field quantities (4) indicates that.

III.3. *CAM-8 Cellular Automata Machine Implementation*

All of our computational investigations of cellular automata utilize the CAM-8 cellular automata machine [1]. CAM-8 can be considered as a personal cellular automata super-computer and consists of about 2 MBytes of SRAM and 64 MBytes of DRAM. A SUN workstation acts as its host. The machine is capable of performing 200M site updates per second on a space of 32M sites.

The updating of sites is performed by table look-up. The binary variables which belong to a particular 16-bit site are passed from DRAM memory through a look-up table stored in SRAM, and then placed back into the same DRAM memory location. Movement of data corresponding to the bit-fields within the site is accomplished through DRAM address manipulation. For the case of CAM-8 evaluation of a LGA, the collision operator is compiled into a look-up table and the advection events performed via DRAM address manipulation [1].

To implement the LGA described in Subsections III.1 and III.2, each field location in the mesh is assigned to an individual CAM-8 site. The allocation of bits used to encode the LGA is shown in Table II. Note that for this initial implementation we exceed the first subcell by 1 bit, and therefore require the use of a single additional subcell. This leaves plenty of bits available in the second subcell for implementing rest particles, material markers, source markers, random bits, etc.

The implementation described in Table II is selected to minimize computational complexity, although it is inefficient in terms of memory storage. For instance, at an E_x site, there

TABLE II
Bit Allocations for CAM-8 Implementation

Bits	Usage
	Subcell 0
0–3	x-directed moving particles
4–7	y-directed moving particles
8–11	z-directed moving particles
12–14	Three-bit cell marker (6 types of cells, $E_x, E_y, \ldots, H_z$)
15	PEC boundary marker
0–7	Also reused as counting bits
	Subcell 1
0–14	Not used
15	Marker for counting window

exists 8 moving particles (see Fig. 4) $b^{\pm}_{\pm y}(\mathbf{x}, t)$, $b^{\pm}_{\pm z}(\mathbf{x}, t)$. However, 12 bits are allocated in Table II to describe this site resulting in 4 unoccupied bits per site. As well, allocating each field location to a CAM-8 site, and hence using a marker to denote the site type, is also wasteful. The LGA cell of Fig. 4 requires a 2 by 2 by 2 region of CAM-8 sites. Two of every eight CAM-8 cells contain a null-cell at which there never exists information.

Although memory inefficient, the implementation described above is relatively easy to develop in a programming sense. Data movement is easily accomplished. The algorithm is easily parsed into different look-up tables for boundary condition implementation, particle collisions, intercell polarization operations, and event-counting. Separation of these events, with a single data transfer event between the collision and event counting table scans, allows for easy testing. In the final implementation, in order to improve computational speed only two look-up tables and therefore two scans of the computational space are required. One is to perform the boundary condition implementation, particle collisions, and intercell polarization operations, and the other is for the event counting.

Both perfect electric conducting (PEC) and perfect magnetic conducting (PMC) boundary conditions have been implemented. These are enforced through locally setting the tangential electric (for PEC) and tangential magnetic (for PMC) fields equal to zero. An electric (magnetic) field component at an E_ξ (H_ξ) site is set to zero by reversing the polarization of the positive and negative particles.

One possible assignment of the three-bit cell marker is

Marker bits	Field component
0 0 0	E_x
0 0 1	H_x
0 1 0	E_y
0 1 1	H_y
1 0 0	E_z
1 0 1	H_z
1 1 0	Null
1 1 1	Null

TABLE III
Percent Error in Resonant Frequency Predicted by the LGA Simulation of TE and TM Modes [17]

Simulation	Modes	Size of space	% error TE, TM solution
1	TE_{111}, TM_{111}	$(128)^3$	0.12, 0.12
2	TE_{121}, TM_{222}	$(128)^3$	0.08, 0.12
3	TE_{121}, TM_{222}	(128, 128, 256)	0.82, 0.12
4	TE_{112}, TM_{321}	(128, 128, 256)	0.15, 0.27
5	TE_{111}, TM_{221}	(256, 256, 128)	0.75, 0.09

IV. NUMERICAL VALIDATION

In this section, the LGA is validated through calculations of the resonant frequencies of various cavities. The first problem considered is the simultaneous solution of both TE and TM modes within a rectangular PEC cavity. TE or TM modes within a rectangular PEC cavity can be individually described by their scalar potential functions, $\varphi_{\text{mnp}}^{TE}$ and $\varphi_{\text{mnp}}^{TM}$ (13) [17], with appropriate boundary conditions imposed on them. These boundary conditions can be enforced through setting the tangential component of the electric field to zero on the cavity walls. This condition is imposed differently on the two scalar potential functions, since the components of the electric fields are derived differently (see (13a) and (13b)). Therefore, a simulation involving both TE and TM modes with boundary conditions enforced on the field components cannot yield correct results without the capability of solving Maxwell's equations. In Table III, results obtained from various simulations are provided. To compute the resonant frequencies, a discrete Fourier transformation of the transient response was computed and peaks in the frequency spectrum were identified with the various modes. In each simulation, TE and TM modes are excited within cavities of various sizes, and the resonant frequencies are compared to the exact solutions. The results indicate that the resonant frequencies of the TE and TM modes are accurately predicted by our LGA for a variety of different mode numbers and simulation space sizes. The errors provided in Table III are less than one percent. The results were obtained from single LGA simulations. Ensemble averaging of LGA simulations might improve the predicted resonant frequencies. Ensemble averaging is more efficient than space-time averaging in the postprocessing of LGA results. Examination of the field distributions produced by the LGA would be efficiently examined using ensemble averaging.

The present capacity of our machine is 64 MBytes and therefore permits a maximum space size of (256 CAM-8 sites)$^3 \rightarrow 256 * 256 * 256 * (2\text{sites}) * 2$ Bytes/site $\sim$64 MBytes. This refers specifically to CAM-8 sites. The number of LGA unit cells (as displayed in Fig. 4) is therefore 128^3. The simulations were run for 4,000 time steps.

The initial conditions for each analysis were enforced through the specification of H_z and E_z field distributions throughout the simulation space. The distribution function for TM_{mnp} and TE_{mnp} modes with subsequent definitions for the electric and magnetic field components are [17]

$$\varphi_{\text{mnp}}^{TM} = \sin\left(\frac{m\pi x}{a}\right)\sin\left(\frac{n\pi y}{b}\right)\cos\left(\frac{p\pi z}{c}\right); \qquad m, n = 1, 2, \ldots; \; p = 0, 1, 2, \ldots$$

$$E_x = \frac{1}{\hat{y}}\frac{\partial^2\varphi}{\partial x\,\partial z}, \qquad E_y = \frac{1}{\hat{y}}\frac{\partial^2\varphi}{\partial y\,\partial z}, \qquad E_z = \frac{1}{\hat{y}}\left(\frac{\partial^2}{\partial z^2} + k^2\right)\varphi \tag{13a}$$

$$H_x = \frac{\partial\varphi}{\partial y}, \qquad H_y = \frac{\partial\varphi}{\partial x}, \qquad H_z = 0$$

and

$$\varphi_{\text{mnp}}^{TE} = \cos\left(\frac{m\pi x}{a}\right)\cos\left(\frac{n\pi y}{b}\right)\sin\left(\frac{p\pi z}{c}\right);$$

$$m, n = 0, 1, 2, \ldots; \; p = 1, 2, \ldots, m = n \neq 0$$

$$E_x = -\frac{\partial\varphi}{\partial y}, \qquad E_y = \frac{\partial\varphi}{\partial x}, \qquad E_z = 0 \tag{13b}$$

$$H_x = \frac{1}{\hat{z}}\frac{\partial^2\varphi}{\partial x\,\partial z}, \qquad H_y = \frac{1}{\hat{z}}\frac{\partial^2\varphi}{\partial y\,\partial z}, \qquad H_z = \frac{1}{\hat{z}}\left(\frac{\partial^2}{\partial z^2} + k^2\right)\varphi,$$

respectively, where $\hat{y} = j\omega\mu$, $\hat{z} = j\omega\varepsilon$, and $k = \pi\sqrt{(m/a)^2 + (n/b)^2 + (p/c)^2}$.

We have also analyzed a finned waveguide using the LGA. Although this is actually a two-dimensional problem, we have utilized the three-dimensional automaton to analyze it. The fin-line cross-section is aligned in the $x - y$ plane, and a short simulation space in the z direction is used (with a wrap-around boundary condition used to terminate the $z =$ minimum and $z =$ maximum planes). A complete description of these numerical simulations is provided in [9]. The problem has been previously investigated with the symmetric condensed node (SCN) TLM algorithm by Herring and Hoefer [18]. The geometry is specified by $a = 2b$, and the resonant frequency is computed for various gap sizes, d. A benchmark solution was obtained through the use of the SCN-TLM algorithm with a lattice size of 256 by 128 Δl [19]. The results are summarized in Fig. 7, and indicate possible values for the LGA to TLM mesh ratios. This problem is an interesting one to carry out a meaningful comparison on because it is simple enough to allow rigorous computational investigation, yet clearly distinguishes between dispersive errors and errors due to imperfect modeling of a spatial field distribution. The discretizations (for the TLM and FDTD analysis) are such that numerical dispersion should be minimal. As discussed, the LGA results are free of numerical dispersion; however, they possess numerical dissipation, similar to that due to Lax–Wendroff style finite-difference or finite-element algorithms [20]. The errors in the determination of cut-off frequency demonstrated in Fig. 7 are due to the inability of the algorithms to accurately predict the behavior of the EM field distribution around the fin. As expected, as the gap size increases (size of the fin decreases), the errors for all discretizations are minimized. We can see in Fig. 7 that the solutions for a TLM mesh of 32 by 16 cells provides the same accuracy as a LGA mesh of 2048 by 1024 CAM-8 sites. The 2048 by 1024 CAM-8 sites correspond with 1024 by 512 LGA cells, and therefore the ratio of LGA to TLM cells required for equivalent accuracy is approximately 30 : 1 per linear dimension of the problem.

The final problem examined is a short cylindrical perfect electric conducting (PEC) cavity. This particular problem adds the twist of requiring a stair-stepped discretization of

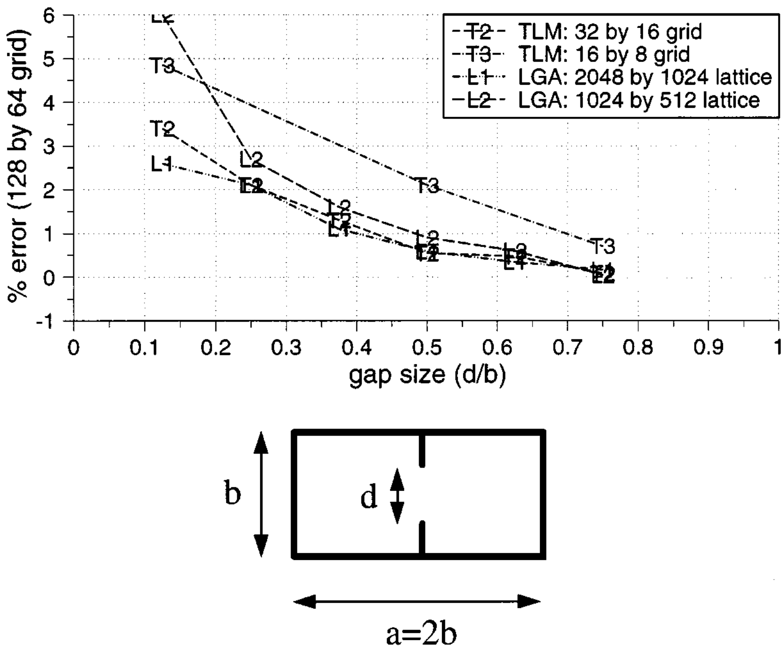

FIG. 7. Percent error in determination of the resonant frequency of the dominant mode versus gap size for various TLM and LGA simulations utilizing different mesh spacing.

the cylindrical surface. This problem is convenient since an analytic solution exists. The cylinder was embedded within a CAM-8 space of size 128 by 128 by 8 sites. The LGA results are compared to stair-stepped FDTD results provided in [21]. The spatial cell size within the automaton is 0.01 m, as compared to 0.05 m within the FDTD results provided by [21]. This 5 : 1 LGA to FDTD mesh ratio is much smaller than that indicated by the finned waveguide analysis. It should be noted that a stair-stepped FDTD analysis does not represent the current state-of-the-art. In fact, the results provided in [21] were actually presented in order to demonstrate the accuracy of their conformal-style algorithm which reduces stair-stepping errors. Their "corrected" resonant frequencies differ from the analytic results by less than 0.1%. We compare the LGA to the stair-stepped FDTD results here to indicate one advantage of the fine discretization required by the LGA (see Table IV). The special treatment of curved PEC boundaries and perhaps even curved material boundaries (which

TABLE IV
Comparison of % Error in LGA Results and Stair-Stepped FDTD Results from [21]

Diameter (m)	% error LGA	% error stair-stepped FDTD
1.00	0.29	2.53
1.03	0.36	2.38
1.05	0.46	4.36
1.07	0.76	3.18
1.10	0.46	1.95

have not received a lot of attention) is not necessary within LGA. Fitting a numerical mesh to a geometrically complex object is not a simple task. Due to the extremely fine spatial discretization associated with LGA, accurate spatial description of PEC boundaries is achieved by default.

Moreover, all of the results indicate that the numerical dispersion of the LGA is very small, for the discretization we have selected. However, numerical dissipation is present in all of these simulations, in the form of a bulk viscosity. This is a result of using fluid-like collision rules (HPP collisions). As expected, the viscosity we have observed is anisotropic [6], and, examining the decay of various modes in various sized simulation spaces indicates it is in the range of 0.07 to 0.50 $\Delta l^2/\Delta t$.

The results of this section indicate the success of the LGA to compute solutions to EM field problems. The present validation does not, however, prove that the LGA is a consistent or convergent method for solving Maxwell's equations. In this paper we have not proved analytically that the model reproduces Maxwell's equations in the macroscopic limit. This proof is eventually necessary and is a topic of our current research [22].

In this paper, we have only addressed EM field problems with homogeneous material properties. Most general problems will possess heterogeneous material regions. We have modeled EM wave interaction with complex heterogeneous objects including a human body cross section in two dimensions using LGA [7, 8]. The LGA described in [7, 8] is based on the addition of rest particles to the HPP automaton. These modified HPP LGA can be implemented in the same way as the standard HPP automata have been implemented in this paper, in order to obtain an LGA for modeling heterogeneous three-dimensional EM field problems.

The increased mesh density required by the LGA is largely due to the presence of numerical viscosity. The viscosity has a large impact on problems with rapid spatial variation of the field distributions. These variations occur in the vicinity of sharp edges such as that encountered with the finned waveguide which results in a LGA to TLM cell ratio of 30 : 1. Although we are utilizing only single-bit variables such an increase in mesh density will result in impractical memory requirements. The reduction of this viscosity is extremely important for the practical application of LGA for EM field modeling. We have investigated integer LGA (ILGA) utilizing low-precision integer variables (4 bits per variable). Theoretical and numerical investigation of these ILGA have indicated a significant decrease in the LGA mesh density required for the finned waveguide problem (from 30 : 1 to 3 : 1 [23, 24]). This results in a decrease in the number of cells by a factor of one thousand. This development allows for the practical application of LGA to the modeling of spatially heterogeneous three-dimensional EM field problems.

V. CONCLUSIONS

In this paper, we describe a LGA for modeling three-dimensional EM field problems. The automaton utilizes particles which possess mass, momentum, and polarization. Conservation of mass and momentum is maintained through utilization of HPP collision events at individual sites, and polarization transformations are applied to maintain correct polarization information for particles travelling to adjacent sites. The new automaton utilizes an expanded spatial cell representation which allows for reasonably simple implementation on a CAM-8 machine. This three-dimensional interconnection of two-dimensional cells is reminiscent of that utilized by the Yee FDTD algorithm [14], the expanded TLM algorithm

[10], and the spatial network method [25]. The numerical results indicate the success of the automaton in analyzing three-dimensional EM field problems.

ACKNOWLEDGMENTS

The authors acknowledge financial support from the Defense Research Establishment Ottawa, Dr. Norm Margolus of MIT's Lab for Computer Science for assistance with the operation of CAM-8, and Mr. Hien Doky for a thorough review of this manuscript.

REFERENCES

1. N. Margolus, CAM-8: A computer architecture based on cellular automata, in *Pattern Formation and Lattice Gas Automata* (Amer. Math. Soc., Providence, 1995).
2. A. Taflove, *Computational Electrodynamics: The Finite-Difference Time-Domain Method* (Artech House, Norwood, MA, 1995), p. 70.
3. P. P. Silvester and G. Pelosi (Eds.), *Finite Elements for Wave Electromagnetics: Methods and Techniques* (IEEE Press, Piscataway, NJ, 1994).
4. C. Christopoulos, *The Transmission Line Modelling Method* (IEEE Press, Piscataway, NJ, 1993).
5. *Proceedings of the Sixth International Conference on Discrete Methods for Fluid Machanics* (Boston, MA, 1996).
6. G. D. Doolen, U. Frisch, B. Hasslacher, S. Orszag, and S. Wolfram (Eds.), *Lattice Gas Methods for Partial Differential Equations* (Santa Fe Institute, 1990).
7. N. Adnani, *Cellular Automata Models for the Two Dimensional Scalar Wave Equation*, M.Sc. Thesis, University of Manitoba, 1996.
8. D. Cule, *HPP Lattice Gas Automata for Computational Electromagnetics*, M.Sc. Thesis, University of Manitoba, 1998.
9. N. R. S. Simons, N. Adnani, G. E. Bridges, and M. Cuhaci, On the potential use of cellular atomata machines for electromagnetic field solution, *Int. J. Numer. Modelling* **8**, 301 (1995).
10. S. Akhtarzad and P. B. Johns, Solution of Maxwell's equations in three space dimensions and time by the TLM method of numerical analysis, *Proc. Inst. Elec. Eng.* **122**, 1344 (1975).
11. P. B. Johns, A symmetric condensed node for the TLM method, *IEEE Trans. MTT* **35**, 370 (1987).
12. N. R. S. Simons and J. LoVetri, Derivation of two-dimensional TLM algorithms on arbitrary grids using finite element concepts, in *First International Workshop on Transmission Line Matrix (TLM) Modelling—Theory and Applications, Victoria, Canada, 1995,* p. 47.
13. C. Adler, B. M. Boghosian, E. G. Flekkoy, N. Margolus, and D. H. Rothman, Simulating three-dimensional hydrodynamics on a cellular-automata machine, *J. Statist. Phys.* **81**, 105 (1995).
14. K. S. Yee, Numerical solution of initial boundary value problems involving Maxwell's equations in isotropic media, *IEEE Trans. Antennas Propagation* **14**, 302 (1966).
15. V. Shankar, W. F. Hall, and A. H. Mohammadian, A time-domain differential solver for electromagnetic scattering problems, *Proc. IEEE* **77**, 709 (1989).
16. J. Hardy, O. de Pazzis, and Y. Pomeau, Molecular dynamics of a classical lattice gas: Transport properties and time correlation functions, *Phys. Rev. A* **13**, 1949 (1976).
17. R. F. Harrington, *Time Harmonic Electromagnetic Fields* (McGraw–Hill, New York, 1961).
18. J. L. Herring and W. J. R. Hoefer, Accurate modelling of zero thickness septa with the symmetric condensed node, *First International Workshop on Transmission Line Matrix (TLM) Modelling—Theory and Applications, 1995*, p. 237.
19. N. R. S. Simons, R. Siushansian, J. LoVetri, and M. Cuhaci, Comparison of the transmission line matrix and finite difference time domain methods for a problem containing a sharp metallic edge, *IEEE Trans. MTT*, in press.
20. J. J. Ambrosiano, S. T. Brandon, and C. R. DeVore, Electromagnetics via the Taylor–Galerkin finite element method on unstructured grids, *J. Comput. Phys.* **110**, 310 (1994).

21. J. Anderson, M. Okoniewski, and S. S. Stuchly, 3D FDTD treatment of perfect electric conductors, in *Proceedings Piers'95, Seattle, WA, July, 1995*, p. 257.

22. M. Zhang, *Derivation of Maxwell's Equations from Lattice Gas Automata, Candidacy Document for* Ph.D. *Degree*, University of Manitoba, 1998.

23. G. E. Bridges and N. R. S. Simons, Extremely low-precision integer cellular array algorithm for computational electromagnetics, *IEEE Microwave and Guided Wave Lett.* **9**, 1 (1999).

24. J. R. Treurniet, G. E. Bridges, N. R. S. Simons, and M. Cuhaci, Evaluation of dissipation within an ILGA for computational electromagnetics, *Int. J. Numer. Modelling*, in press.

25. N. Yoshida and I. Fukai, Transient analysis of a stripline having a corner in three-dimensional space, *IEEE Trans. MTT* **32**, 491 (1984).